
DESIGN AND PERFORMANCE OF THE BEAMLET OPTICAL SWITCH

M. A. Rhodes

L. J. Atherton

B. W. Woods

C. L. Robb

J. J. DeYoreo

D. H. Roberts

Introduction

High-energy lasers for Inertial Confinement Fusion (ICF) experiments are typically designed with large apertures (>30 cm) to keep the fluence below the damage threshold of the various optical components. Until recently, no optical switch technology could be scaled to the aperture size, aperture shape (square), and switching speed required for the next generation of ICF drivers. This step is critical: The Beamlet multi-pass amplifier cavity uses a full-aperture optical switch to trap the laser pulse within the cavity and to divert the pulse out of the cavity when it reaches the required energy.¹ By rotating the polarization of the beam, a Pockels cell in the switch controls whether the beam is transmitted through, or reflected from, the polarizer.

In conventional Pockels cells, a longitudinal electric field is applied to an electro-optic crystal via external ring-electrodes.² To achieve a reasonably uniform field distribution in the crystal, the crystal's aspect ratio (diameter:length) must be no greater than 1:1 (1:2 is preferable). Since the required aperture in high-energy ICF drivers is in the range 30 to 40 cm, the crystal would have excessive optical absorption, strain depolarization, and cost. One alternative Pockels cell design approach, which allows for thin crystals, employs transparent, conductive thin films applied to the crystal surfaces as electrodes.³ Unfortunately, such films exhibit insufficient conductivity to meet our switching speed requirements and do not have a high enough optical damage threshold.

In this article, we describe an optical switch technology that does scale to the required aperture size and shape for Beamlet and the proposed National Ignition Facility (NIF) laser, and can employ a thin crystal. This switch consists of a thin-film polarizer and a plasma-electrode Pockels cell (PEPC), the latter originally invented at Lawrence Livermore National Laboratory (LLNL) in the 1980s⁴ and under further development

since 1991. After discussing the PEPC concept, we present the design and optical performance of a 32×32 cm² prototype PEPC, including discussions of the crystals, the PEPC assembly, the vacuum and gas system, and the high-voltage pulsers. Then we describe the performance of the 37×37 cm² PEPC constructed specifically for the Beamlet laser. Finally, we discuss important technology issues that arose during PEPC development: cathode sputtering, cathode heating, nonuniformities in the switching profile, switch-pulse leakage current, and an estimate of the plasma density and temperature produced during PEPC operation.

The Plasma-Electrode Pockels Cell Concept

Figure 1 shows a top view cross-section of a PEPC and a simplified schematic of the required external electronic circuit. Vacuum regions on each side of the crystal are filled with working gas (He + 1% O₂) at an optimized operating pressure (30–40 mTorr). The plasma pulsers ionize this gas with a high-current pulse, forming the plasma-electrodes. Voltage from the switch pulser is applied across the crystal via these plasma-electrodes. As in a conventional Pockels cell, if the potential difference across the crystal is V_π , the half-wave voltage, the polarization of an incoming linearly polarized beam is rotated by 90°. For the crystals considered here, potassium dihydrogen phosphate (KDP) and potassium dideuterium phosphate (KD*P), V_π is 16.4 kV and 6.5 kV (at 1.06 μ m optical wavelength) respectively.⁵

Requirements on the plasma and switch pulsers are set by the switching speed requirement placed on the PEPC, which depends on the particular application. In the Beamlet laser, the optical pulse propagates through

the amplifier cavity for two round trips, leading to four passes through the amplifier. The PEPC and the polarizer function together as an optical switch that controls the state of the cavity. If the cavity is closed, the optical pulse and any amplified stimulated emission are trapped within the cavity. If the cavity is open, the optical pulse is switched out of the cavity. The polarizer is arranged so that the cavity is open when no voltage is applied to the PEPC crystal and closed when the crystal is charged to V_π . To switch the optical pulse out of the cavity, the PEPC must change state in less than the cavity round-trip transit time, which is approximately 240 ns for Beamlet. We chose 100 ns as the nominal switching speed to allow extra time for voltage equilibration across the crystal aperture. The time constant by which the voltage on the crystal changes is given by $\tau = Z_{sw} C_{KDP}$, where Z_{sw} is the effective impedance of the switch pulser (parallel combination of the pulser output impedance and the terminating resistance) and C_{KDP} is the capacitance of the crystal. The Beamlet crystal is $37 \times 37 \text{ cm}^2$ and 1 cm thick and consists of ordinary KDP with a relative dielectric

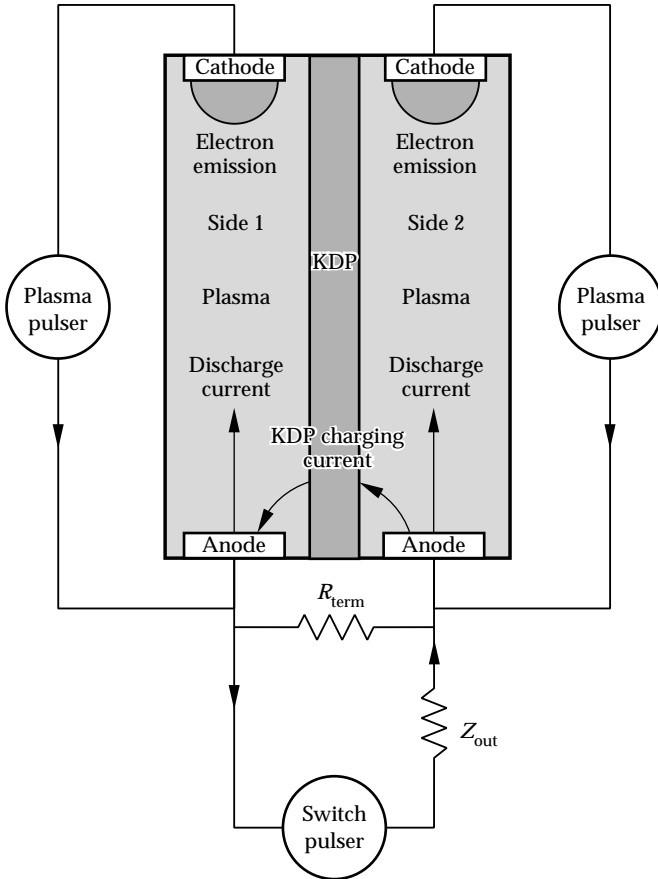


FIGURE 1. A top-view cross-section of the PEPC and its associated electronic circuit. The plasma pulsers produce the plasma electrodes by high-current discharge in He; the switch pulser then applies the switching voltage across the KDP crystal. (70-50-1294-3986pb01)

constant $\epsilon_r = 20$. We calculate the crystal capacitance by assuming a simple parallel-plate geometry and obtain $C_{KDP} = 2500 \text{ pF}$. It takes four time constants to charge the crystal to 98% of V_π , so τ must be one-fourth of our desired switching speed, or 25 ns. This implies that Z_{sw} must be 10Ω , and this determines the peak current I_{sw} that must be delivered by the switch pulser: $I_{sw} = V_\pi / Z_{sw} = 1.7 \text{ kA}$. If a KD*P crystal is used, the capacitance is higher because $\epsilon_r = 50$. An impedance of 4.0Ω is required to achieve the same 25-ns time constant. The peak current requirement is about the same (2.0 kA) because of the lower V_π for KD*P.

The plasma current I_p at the time the switch pulse is fired must be greater than I_{sw} ; otherwise the current from the switch pulser charging the crystal clamps at I_p , which increases the time required to fully charge the crystal.⁶ This effect is due to the diode-like nature of the plasma discharge. Figure 1 depicts the discharge current and the KDP charging current. On side 2, the plasma and switch-pulse currents are in the same direction; on side 1 they are in opposite directions, so they cancel. If the peak switch-pulse current is greater than the plasma current, the current at the side 1 anode must go negative, which means that it is emitting electrons. This cannot happen on the time scale of the switch pulse.

A circuit model, shown in Fig. 2, was used to determine the relation between peak switch-pulse current and the plasma current. We model each plasma with a $0.1\text{-}\Omega$ resistor in series with a diode, and we model the crystal capacitance with a 2500-pF capacitor. We set the value of the resistors to be on the order of the plasma collisional resistivity (see below), which is much smaller than Z_{sw} . We model the plasma currents with a pair of

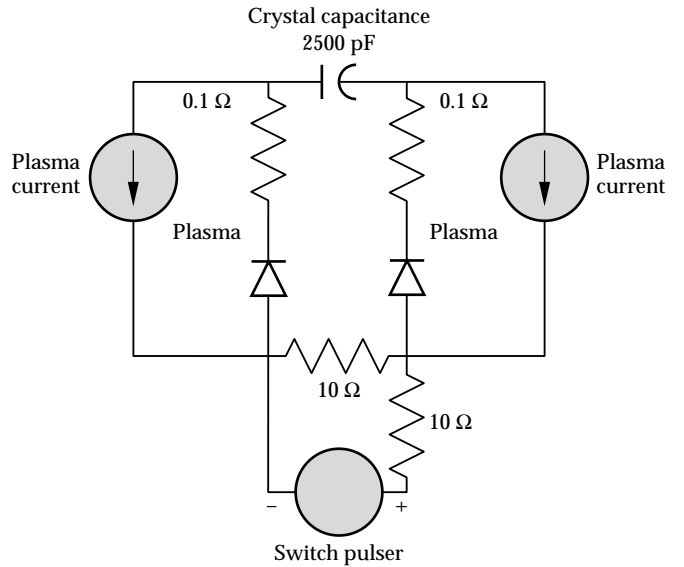


FIGURE 2. Circuit model of the PEPC used to determine the relation between peak switch-pulse current and plasma current (results shown in Fig. 3). (70-50-1294-3980pb01)

current sources; the switch-pulse voltage is applied by a 20-kV rectangular pulse source with a 10-Ω series resistor to model Z_{sw} . Using PSPICE⁷ to calculate the circuit response, we find the peak charging current for this case is 2 kA, so the plasma current must be greater than 2 kA if it is not to limit the crystal charging time. Figures 3(a) and 3(b) show the model results for the crystal charging current and voltage, respectively, for cases when the plasma current is 2.0 and 0.5 kA. For the 2-kA case, the current in the crystal peaks at slightly <2 kA (because of the plasma resistance), and the crystal charges with the expected time constant. For the 0.5-kA plasma current case, the charging current clamps at 0.5 kA, extending the charging time. The voltage rise time is longer for the 0.5-kA case.

The preceding analysis puts a lower limit on the required plasma current. In practice, however, we find that optimum performance is achieved at somewhat higher current. This is because the plasma resistance must be small compared to the Z_{sw} assumed in our circuit model, and because the plasma must be sufficiently uniform across the full aperture. Two processes contribute to the plasma resistance: electron scattering by collisions with neutrals and coulomb scattering of electrons by the plasma ions.

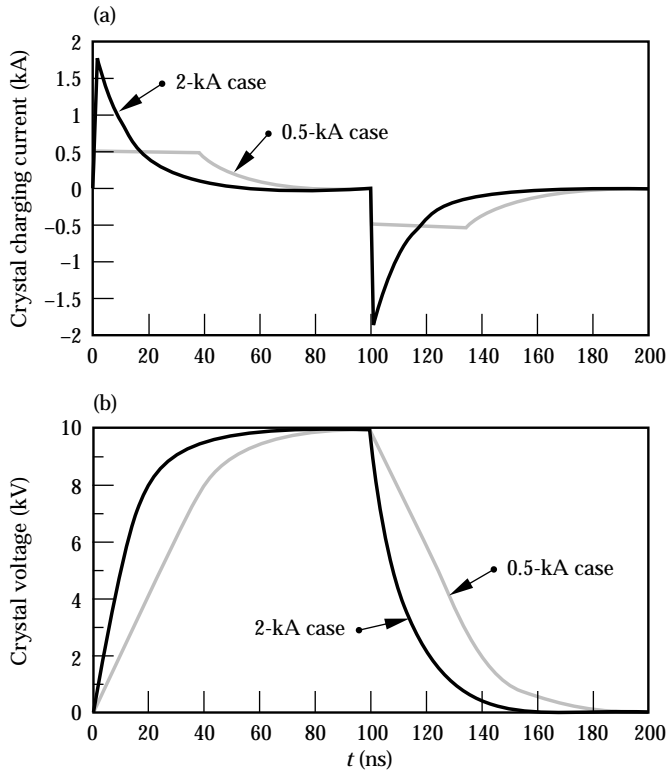


FIGURE 3. (a) Current (based on circuit in Fig. 2) in the crystal capacitance for plasma currents of 2 kA and 0.5 kA. For currents <2 kA, the charging current clamps at the plasma current, extending the charging time. (b) Corresponding voltage waveforms. The voltage rise time is longer for the 0.5-kA plasma current.

(70-50-1294-3981pb01)

The plasma resistivity η_{en} due to electron-neutral collisions is given in Ω-cm by

$$\eta_{en} = 8.93 \times 10^{11} \frac{n_n}{n_e} \left(\frac{m_e \sigma_{en}}{q^2} \sqrt{\frac{kT_e}{m_e}} \right), \quad (1)$$

where n_n is the neutral density, n_e is the electron density, m_e is the electron mass, σ_{en} is the electron-neutral collision cross-section, which we take to be $5.3 \times 10^{-16} \text{ cm}^2$ for He,⁸ kT_e is the electron thermal energy, and q is the electron charge. All quantities are in cgs units.

The resistivity due to coulomb scattering is given by⁹

$$\eta_{ei} = 5.2 \times 10^{-3} \frac{Z \ln \Lambda}{T_{eV}^{\frac{3}{2}}}, \quad (2)$$

where Z is the average ion charge state, and T_{eV} is the electron temperature in electron-Volts. The Coulomb logarithm $\ln \Lambda$ (≈ 10) is a correction term for small-angle scattering.

The relative contribution to plasma resistance from these two processes depends on the operating conditions. Using a method described later, we estimate $n_e = 1.6 \times 10^{12} \text{ cm}^{-3}$ for $T_{eV} = 5 \text{ eV}$. With an operating pressure of 35 mTorr, the plasma resistivity is dominated by electron-neutral collisions, and the total plasma resistance is 0.04 Ω, which is much less than the switch-pulser impedance.

Design of the 32-cm Prototype PEPC

In this section, we describe design details for the PEPC and its associated subsystems, including the crystals, the PEPC assembly, the vacuum and gas supply system, the discharge electrodes, the plasma generation system, and the switch pulser.

Crystals

The original design for the Beamlet PEPC called for a KD*P crystal with a high deuterium concentration (>90%). KD*P is desirable because at 90% deuteration, optical absorption for 1.05-μm light traveling parallel to the crystal z-axis is 0.49%/cm compared to 5.8%/cm for KDP.¹⁰ However, when we began this development work it was not known whether KD*P crystals of sufficient size and quality could be grown for use in the Beamlet PEPC. We constructed a prototype PEPC based on the largest KD*P crystal available at that time ($32 \times 32 \text{ cm}^2$) and tested it with both KDP and KD*P crystals. Before testing in the PEPC, we measured the strain depolarization of both crystals using an experimental setup described elsewhere.¹¹ This apparatus

measures the extinction ratio (ER) point by point across the surface of the crystal under test. From the array of data points, we construct a strain image of the crystal. For consistency, we convert all ER s to effective switching efficiency, S_{eff} , which is given by

$$S_{\text{eff}} = 1 - \frac{1}{ER} . \quad (3)$$

An ER of 100 corresponds to an efficiency of 99% while an ER of 1000 corresponds to an efficiency of 99.9%.

Figure 4 shows the resulting strain images for the KD*P and KDP crystals. The KD*P crystal exhibits more strain structure than the KDP crystal: growth sector boundaries are clearly visible, for example. However, for these particular crystals, the KD*P has slightly higher average efficiency than the KDP (99.987% vs 99.952%) and higher worst-spot efficiency (99.78% vs 99.65%).

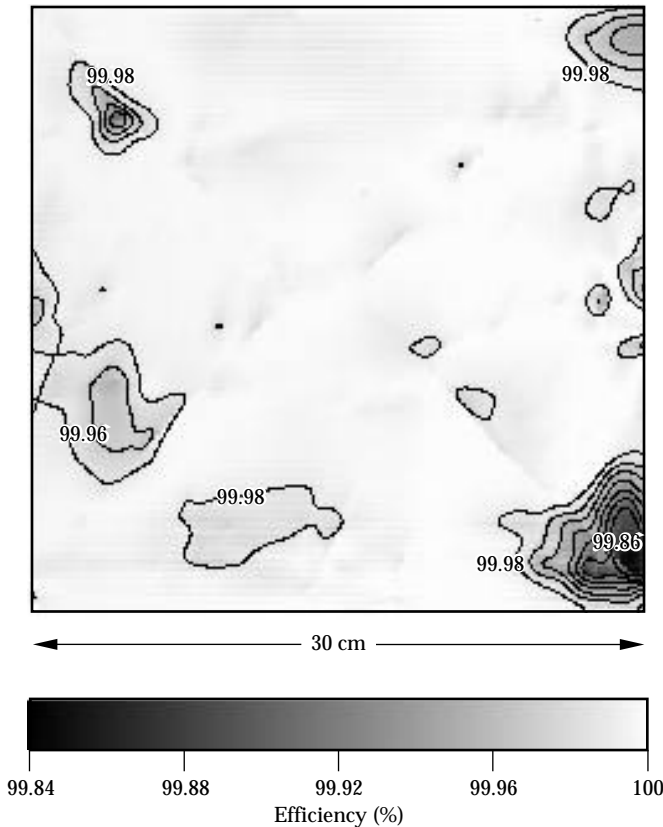


FIGURE 4. Strain map for a $32 \times 32 \text{ cm}^2$ KD*P crystal shown in terms of the switching efficiency (see text for definition). Regions of lower efficiency denote loss due to strain-induced depolarization. (70-50-1294-3982pb01)

PEPC Assembly

Figure 5 shows the PEPC assembly. The crystal is potted into a ceramic frame with silicone elastomer. This frame mounts between two housings, which are in turn sandwiched between two 4-cm-thick fused silica windows. The housings, made from ultrahigh-molecular-weight polyethylene, define the vacuum regions on each side of the crystal. The housings also hold the discharge electrodes in place and interface to the vacuum pumping system. The windows seal the vacuum regions on the outside and allow transmission of the optical pulse. The windows and the KDP crystal are antireflection coated with sol-gel silica particles.¹² The total transmission through the cell was 99.1% with the KD*P crystal and 93.9% with the KDP crystal.

The housing assembly rests on a support structure that provides motorized x and y translation and manual adjustment of tip, tilt, and twist so that we can align the PEPC to our test beam. The support structure also holds the vacuum pumping system.

Vacuum and Gas System

The vacuum and gas system provides the required environment inside the PEPC for optimum formation of the plasma electrodes. A two-stage turbomolecular pump evacuates the PEPC interior to less than 5×10^{-5} Torr. This base pressure ensures that the concentration of impurity species in the plasma is low enough that it does not degrade the discharge uniformity. The gas system injects the working gas (a mixture of He plus 1% O_2) into the cell and maintains the gas pressure at 35 mTorr with active feedback control. The feedback system uses a capacitance manometer to monitor the cell pressure and drives a servo loop actuating a gas metering valve. The operating pressure is maintained by flowing gas while the turbopump continuously evacuates the cell. We discuss the purpose of the oxygen below.

Discharge Electrodes

The plasma electrodes are formed by driving current between pairs of anodes and cathodes. The anodes are simple bars of stainless steel. The cathodes are planar magnetron structures (Fig. 6).¹³ Planar magnetrons are commonly used in direct current and radio frequency discharges as sputtering sources, but to our knowledge this is the first application as a cathode for a high-current pulse discharge.

Permanent magnets beneath the cathode surface provide a closed $\mathbf{E} \times \mathbf{B}$ path for electron flow on the cathode surface, leading to increased plasma density near the cathode. The magnetron cathodes result in lower operating pressure and lower discharge voltage

across the anode-cathode gap than with unmagnetized cold cathodes. The lower operating pressure leads to lower plasma resistivity, as explained in “The Plasma-Electrode Pockels Cell Concept” earlier. Lower discharge voltage leads to less cathode sputtering, less cathode heating, and lower potential differences between the side 1 and side 2 plasmas (higher potential differences are more likely to cause partial optical switching before application of the switch pulse).

During the discharge, He ions from the plasma are accelerated by the discharge potential and bombard the cathode, producing electrons by secondary emission. This electron emission sustains the discharge. However, the ion bombardment also leads to sputtering of the cathode material, which can deposit on the crystal and window surfaces, reducing their optical damage threshold. To eliminate this deposition, the cathode surfaces are made from high-purity graphite, so the sputtered material is C. The sputtered C reacts with the 1% O_2 in the plasma to form CO and CO_2 , which are pumped away by the vacuum system. We describe experimental tests of this process later in this article.

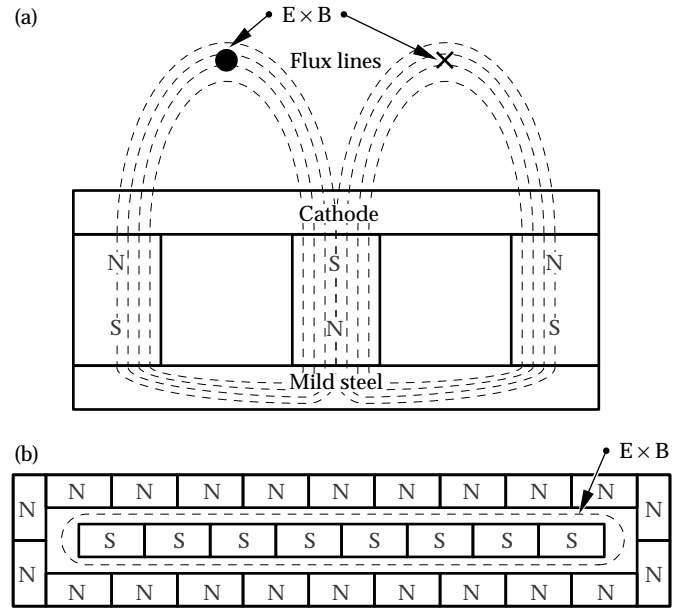


FIGURE 6. (a) Cutaway side view and (b) top view of the magnet layout for the planar magnetron cathodes used in the PEPC. The magnetron cathodes provide a uniform discharge without thermionic emission. (40-00-0494-1608pb01)

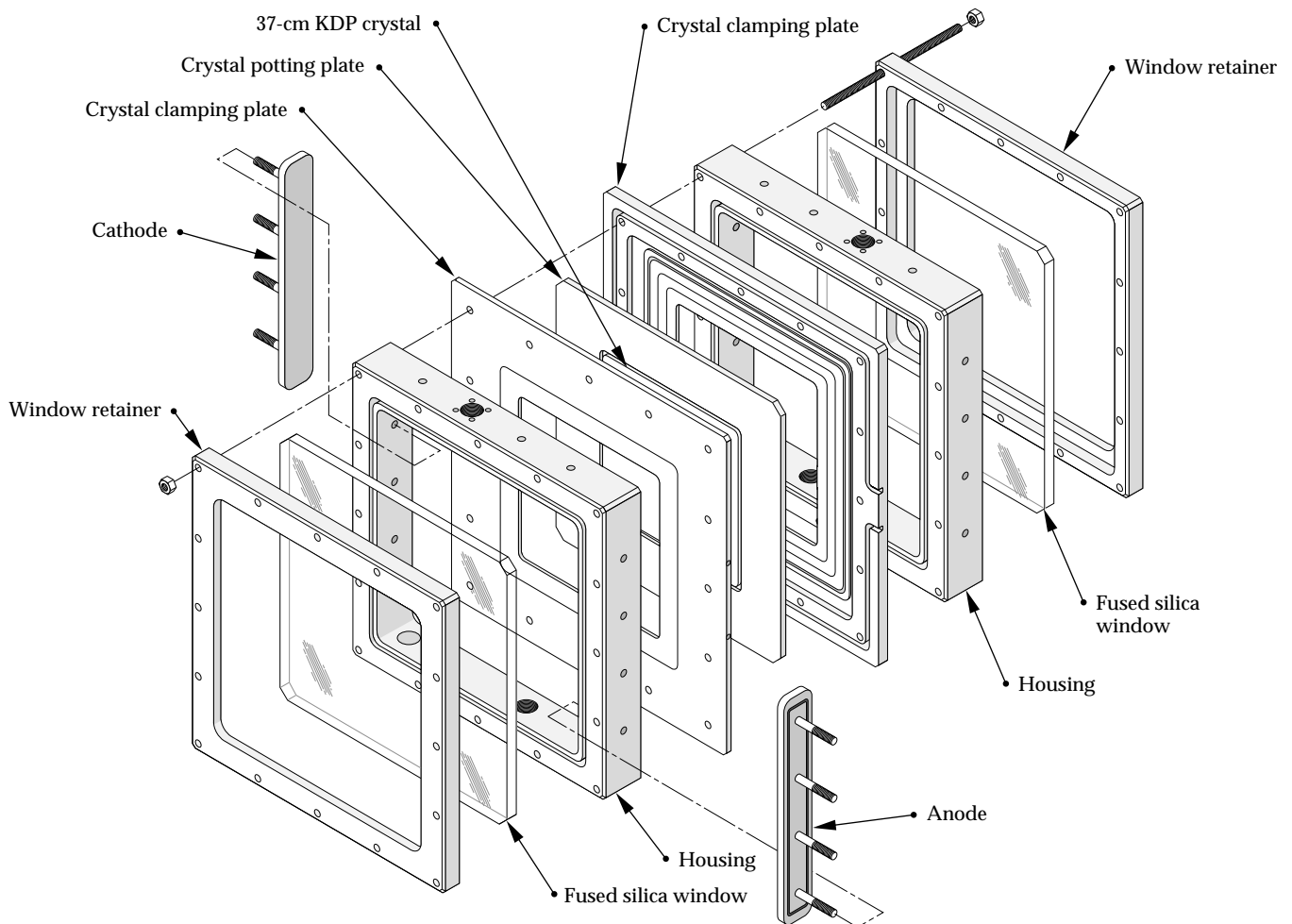


FIGURE 5. Exploded view of the PEPC assembly, showing the sandwich-like structure. (02-30-0391-1444pb01)

Plasma Generation System

The plasma is created in a two-stage process: a low-current preionization (simmer) discharge and a high-current pulsed discharge. The simmer discharge is initiated by a high-voltage, low-current power supply that provides enough voltage to break down the gas (about 1.5 kV) and then provides a constant discharge current of 30 mA. The voltage required to maintain the simmer discharge is about 300 V. The high-current pulse is produced by discharging a 5- μ F capacitor charged to 4 to 7 kV depending on the required peak current. We call the capacitor and low-current power supply the *plasma pulser*. Figure 7 shows a typical plasma current waveform and the relative timing of the switch pulse, which we typically time to fire just after the peak in the plasma current.

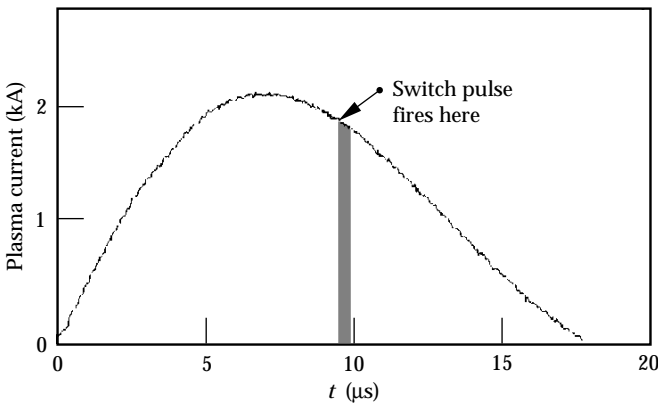


FIGURE 7. Plasma current for a 2-kA pulse, and relative timing of the switch pulse. (70-50-0594-2403pb01)

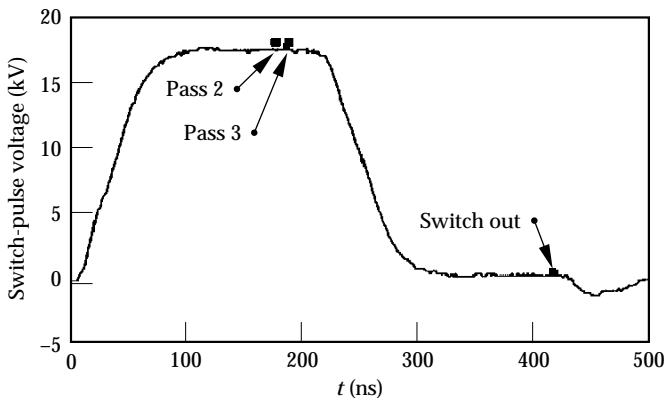


FIGURE 8. Voltage across the PEPC during normal operation, and when the optical pulse traverses the cell—twice when the voltage is on (pass 2 and pass 3) and once after the cell is discharged (switch out). (70-50-0594-2402pb01)

Switch Pulser

The switch-pulse generator¹⁴ produces a nominally rectangular pulse applied across the crystal via the plasma electrodes. The switch pulser satisfies several important requirements: shot-to-shot jitter is <2 ns, a voltage flat-top at least 50 ns long is within $\pm 2\%$ of V_π , and the voltage returns to zero ($\pm 2\%$ of V_π) after the pulse, so that the optical pulse is efficiently switched out of the cavity. The pulse is produced by sections of coaxial cable used as a pulse-forming network (PFN). A high-voltage power supply charges the PFN to twice the required output voltage, and a thyatron switches the charged PFN into the output line, which is also made up of coaxial cable sections. Multiple PFN and output lines are connected in parallel to achieve the switch-pulser impedance required to charge and discharge the crystal in less than the round-trip transit time of an optical pulse in the Beamlet laser-amplifier cavity. The output pulse duration depends on the length of the PFN cables. The output cables are long enough that electrical reflections due to impedance mismatches at the cell do not return to cause voltage ripples until after the required switch-out time.

We can configure the switch pulser for operation with KDP or KD*P. For KDP, we use four 50- Ω PFNs and output lines in parallel to achieve a pulser impedance of 12.5 Ω . For KD*P, we use eight cables in parallel for an impedance of 6.25 Ω . Figure 8 shows a typical voltage waveform produced by the Beamlet switch-pulse generator. Also shown is the relative timing of the optical pulse on the multiple passes through the cell when used in the Beamlet multipass cavity. The laser pulse traverses the cell three times: twice when the voltage is on and once when the voltage is off.

Prototype PEPC Optical Switching Performance

We evaluated the switching performance of the prototype PEPC with both KD*P and KDP crystals. A Q-switched, pulsed laser (10-ns nominal pulse duration at 1.06 μ m) was used as the illumination source. A beam splitter diverted a small portion of the beam into a reference detector. After traversing a polarizer, the beam was expanded with a negative lens and collimated through the PEPC with a 30-cm-diam lens. After traversing the PEPC, a second 30-cm-diam lens focused the beam through an analyzing polarizer. A small-aperture positive lens imaged the plane of the PEPC crystal on the detector. We used two types of detectors: a photodiode to look at average performance across the whole aperture and a charge-coupled device (CCD) video camera to produce images of the

performance in two dimensions. With these optics, we could not illuminate the full $32 \times 32 \text{ cm}^2$ aperture at once; we used the x - y translation capability of our support structure to diagnose the cell in four quadrants.

We define several different ER s to help describe the switching performance. The system extinction, ER_{sys} , is the ratio of the detected intensity with the polarizers aligned to the intensity with the polarizers crossed without activating the PEPC. ER_{sys} is a measure of depolarization errors in the various optical components. With the beam at small aperture (only the polarizers in the beamline with no expansion optics), we find $ER_{\text{sys}} > 1 \times 10^5$. Adding the expansion, collimating, and imaging lenses reduces ER_{sys} to about 3000. Adding the PEPC into the beamline further reduces ER_{sys} to about 1500 because of strain in the windows and crystal.

During PEPC operation, we measure ER_{on} , the ER when the voltage is on, and ER_{off} , the ER in the switch-pulse tail at the time of switch-out (about 200 ns after the end of the switch pulse). ER_{on} is the ratio of light intensity incident on the PEPC to the light intensity that remains unrotated with the PEPC at V_π . We measure ER_{on} with the polarizers aligned and take the ratio of the detector signal with no voltage on the PEPC to the signal with V_π on the PEPC. Although the switch pulser does a good job of discharging the crystal, some residual charge remains on the crystal at the critical switch-out time, leading to an ER_{off} lower than ER_{sys} . We measure ER_{off} by taking the ratio of the detector signal with the polarizers aligned and no voltage on the switch to the detector signal with the polarizers crossed, 200 ns after the trailing edge of the switch pulse as already defined.

As before, we express the data in terms of efficiency. S_{off} represents the percentage of light that would be switched out of the cavity on pass 4, while S_{on} is the percentage of light that stays in the cavity for gain passes 2 and 3. The goals for S_{on} and S_{off} set at the beginning of the development program, were $>99\%$ ($ER=100$) average across the aperture and no spots worse than 98% ($ER=50$). These efficiencies include only losses due to depolarization of the beam and do not include losses due to surface reflections and absorption.

Figure 9 shows a typical S_{on} image of the prototype PEPC with a KDP crystal. In this example, S_{on} in the worst spot is 99.64% . Table 1 summarizes switching performance with our 30-cm-diam imaging aperture centered on the PEPC for KDP and KD*P. The performance exceeds the required performance for both KD*P and KDP. The shot-to-shot reproducibility is indicated by the standard deviations of the average efficiencies. We obtained the average efficiencies by averaging 10 or more consecutive photodiode signals (with the system operating at a consistent 0.25 Hz). We obtained the worst-spot results by scanning images acquired with our CCD video system for each condition.

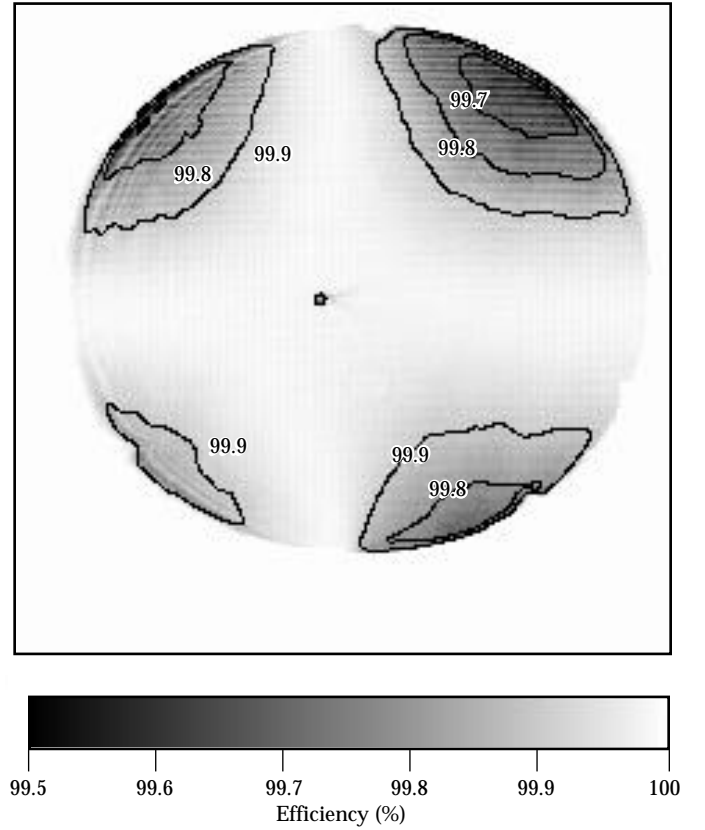


FIGURE 9. Typical S_{on} efficiency image from the prototype PEPC with a $32 \times 32 \text{ cm}^2$ KDP crystal. A 30-cm-diam central view is shown. (70-50-1294-3983pb01)

TABLE 1. Switching performance of prototype PEPC with KD*P and KDP crystals. Goals were average efficiencies greater than 99% and no spots worse than 98% .

Crystal type	During switch pulse, S_{on}		After switch pulse, S_{off}	
	Average ($\pm 1 \sigma$)	Worst spot	Average ($\pm 1 \sigma$)	Worst spot
KD*P	$99.90 \pm 0.02\%$	99.60	$99.85 \pm 0.02\%$	99.39
KDP	$99.91 \pm 0.01\%$	99.49	$99.91 \pm 0.02\%$	99.64

Design and Optical Performance of the Beamlet PEPC

Based on our experience with the prototype PEPC, we designed and built a PEPC for use in the Beamlet laser. Figure 10(a) shows the Beamlet PEPC fully assembled, and Fig. 10(b) shows it integrated into the Beamlet laser. It is essentially the same as the prototype PEPC, except that it is large enough to accommodate a

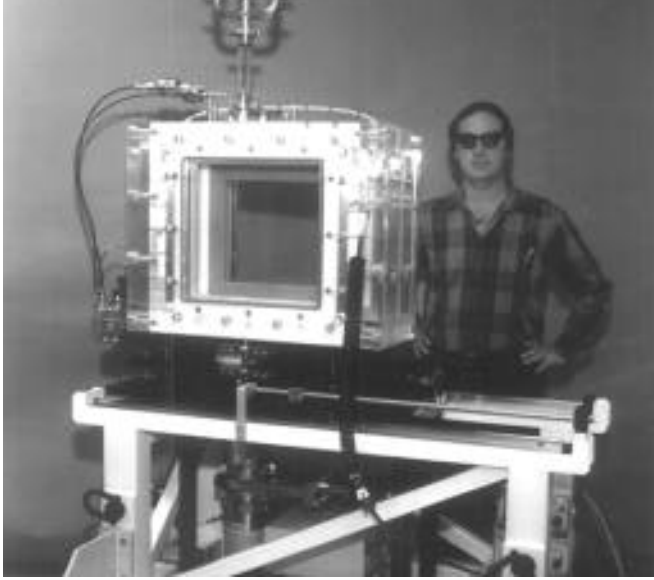
$37 \times 37 \text{ cm}^2$ crystal, the cathodes are set back from the edge of the crystal by 6 cm in a reentrant cavity, and the outer windows are 3 cm thick (they were 4 cm thick in the prototype).

Operation of the Beamlet PEPC as part of the Beamlet laser began in February 1994. Before operation at high optical fluence, we evaluated the switching performance at low fluence using a $32 \times 32 \text{ cm}^2$ KDP crystal. We performed these tests with the PEPC installed into the Beamlet laser cavity and used the Beamlet diagnostic system. Figure 11 shows the experimental setup we used to test the switching performance at low fluence. At the beginning of a Beamlet shot, an optical pulse from the front-end laser is injected into the spatial filter. A small injection mirror (not shown) reflects the pulse toward cavity mirror M_1 through the cavity amplifier (which was not energized for the low-fluence tests). The pulse reflects from M_1 and passes back through the amplifier and spatial filter before it illuminates the PEPC at full aperture (35 cm). After traversing the PEPC, the beam reflects from the polarizer if the PEPC is off and passes through the polarizer if the PEPC is on (as shown in Fig. 11). A portion of the light transmitted by the polarizer passes through the partially transmitting cavity mirror M_2 into the diagnostic system. The sampled pulse is down-collimated by lens L_3 and other small-aperture optics (not shown) that image the crystal plane of the PEPC onto a high-resolution CCD video camera.

We ratio the switch-on and switch-off images to produce a switching efficiency image as shown in Fig. 12. As before, the switching efficiency data includes only losses due to beam depolarization and not losses from surface reflections or absorption. In this low-fluence test, we observed an average switching efficiency across the aperture of 99.5%; the minimum efficiency was 97.5% in the upper left-hand corner. The regions of lower switching efficiency in the corners are caused by strain-induced depolarization in the fused silica windows arising from vacuum loading.

During a full system shot, the cavity amplifier is energized. The voltage pulse applied to the switch starts at about the same time the optical pulse hits the injection mirror. Voltage across the crystal equilibrates while the optical pulse propagates towards mirror M_1 in Fig. 11 and makes its first two gain passes through the amplifier. While passing through the PEPC, the optical pulse polarization rotates by 90° and thus passes through the polarizer. The optical pulse reflects from mirror M_2 and passes through the polarizer and PEPC (rotating another 90°) before it propagates back toward the amplifier for two more gain passes. During this 240-ns interval, the voltage across the PEPC drops to zero. When the optical pulse returns again, the polarization is not rotated by the PEPC, so the pulse

(a)



(b)



FIGURE 10. (a) Beamlet PEPC before installation into the Beamlet laser. (b) Beamlet PEPC integrated into the Beamlet laser.
(70-50-0494-1845pb01)

reflects off the polarizer and out of the cavity. While details of the Beamlet laser performance¹⁵ are not within the scope of this paper, we report that the main Beamlet cavity has produced up to 6 kJ of 1.06- μm light in a 3-ns pulse with switched, four-pass operation. During these tests, the Beamlet PEPC operated reliably and reproducibly, exhibiting high-fluence (average of 5 J/cm²) switching efficiency >99.5% for both cavity-closed and cavity-open states.

PEPC Technology Issues

In this section, we discuss important technology issues that surfaced during our developmental work, including sputtering of cathode material, indirect crystal heating by the cathode, magnetically induced regions of nonuniform switching (bright spots), and switch-pulse leakage current to the vacuum system.

Although we have no direct measurement of the plasma parameters (density and temperature) except for the low-current simmer plasma, we also present in this section a method for estimating the plasma density based on the observed difference between the known V_π for KDP and the applied voltage required to achieve optimum switching. These plasma parameters are required for estimating the plasma resistance.

Sputtered Cathode Material

As mentioned in “Discharge Electrodes” earlier, the gaseous discharges that form the plasma electrodes sputter the cathode material. In an early cathode design, we used Mo for the cathode surface because of its relatively high secondary-electron emission coefficient under He-ion bombardment. After several thousand shots with this cathode, we illuminated the prototype PEPC with a partially focused beam to test operation at high fluence. Our setup allowed us to vary the fluence to over 25 J/cm². During this test, we imaged the crystal with a telescope and watched for

optical damage as we increased the fluence. We observed a significant reduction in damage threshold near the cathode, while the threshold for other parts of the crystal remained unchanged. We found that this reduction in damage threshold was due to deposition of Mo on the crystal, which was highest near the cathode and decreased with distance from the cathode.

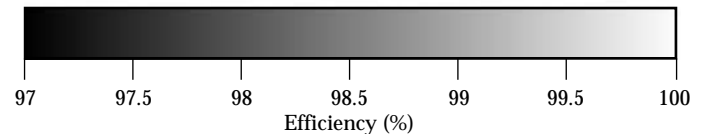
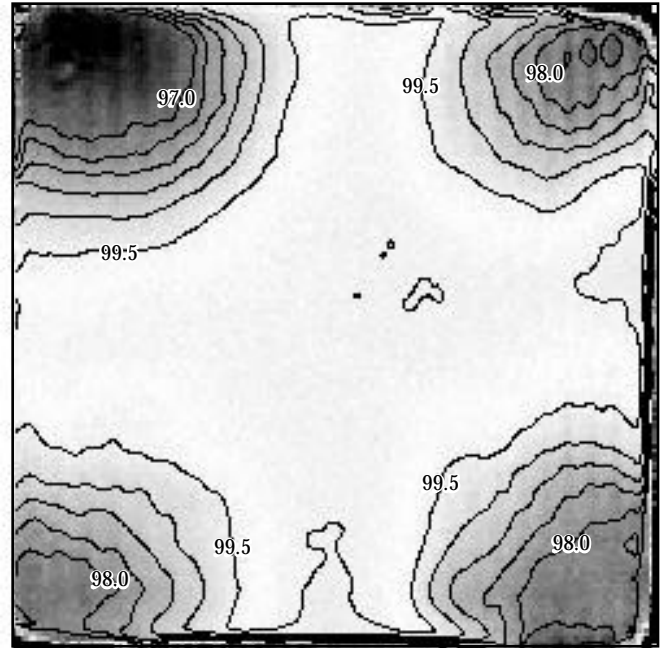


FIGURE 12. Switching efficiency across the 35 × 35 cm² aperture of the Beamlet PEPC. Lower switching efficiency in the corners is due to strain-induced birefringence in the silica windows arising from vacuum loading. (70-50-1294-3984pb01)

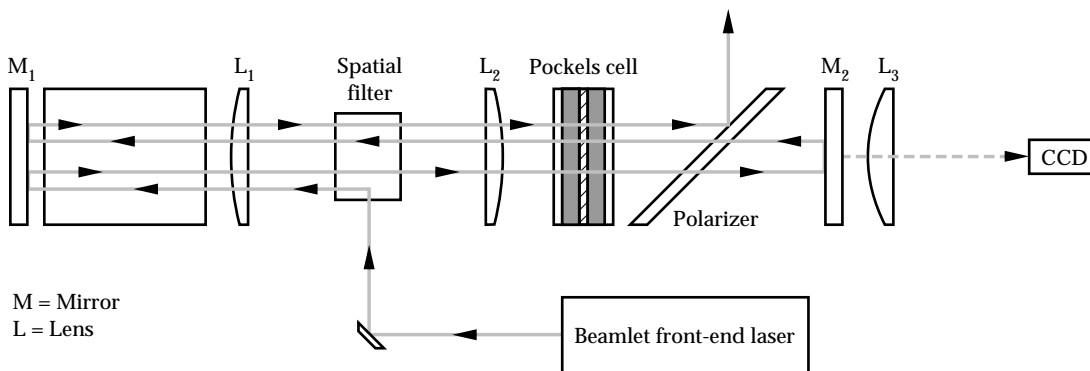


FIGURE 11. Simplified diagram of the experimental setup used to evaluate the switching performance of the PEPC in the Beamlet laser at low fluence. An optical pulse from the Beamlet front-end laser propagates through the PEPC and polarizer. A high-resolution CCD video camera images the light transmitted by the PEPC-polarizer combination. (70-50-1294-3985pb01)

To confirm this sputter coating of the crystal, we exposed witness plates to several thousand shots and detected Mo on the plates with standard analysis techniques, including electron spectroscopy chemical analysis and inductively coupled plasma mass spectroscopy.

We solved this sputtering problem by replacing the Mo cathode covers with high-purity graphite and adding 1% O₂ to the He working gas as described in “Discharge Electrodes.” We confirmed the effectiveness of this technique with three experiments: direct measurement of sputter deposition using a quartz crystal microbalance, observation of CO and CO₂ gas production using residual gas analysis, and optical damage tests performed on witness plates exposed to the plasma.

To monitor the deposition of sputtered material directly, we inserted a quartz crystal microbalance into the prototype PEPC, placing the face of the microbalance 4 cm from the cathode surface. The quartz crystal is coated with a thin Au film and is part of a resonant circuit whose frequency depends on the temperature of the crystal and the mass of material on the crystal face. The sensor frequency is also affected by changes in the ambient pressure, which affects the mass of adsorbed gas on the crystal face. As long as temperature and pressure are held constant, changes in the resonant frequency are due to changes in mass arising from deposition.

The results of an experiment in which we initially ran the discharge with a pure He plasma showed C sputtered from the cathode depositing on the nearby sensor head. Without stopping the discharge, we changed the working gas to a mixture of He plus 1% O₂. Initially, the sensor responded with an apparent step increase in film thickness when the gas was changed. However, the sensor response is actually due to a change in the mass of adsorbed gas. After the sensor reached a new equilibrium, the effective film thickness decreased monotonically as the previously deposited C reacted with the O₂ to form CO and CO₂.

For the second test, we directly measured with a residual gas analyzer the formation of CO and CO₂ during the discharge. We estimated the sputtered flux of C to be 1.1×10^{16} atoms/s for a 23-mA discharge current and a sputtering coefficient of 0.1 for He bombarding graphite.¹⁶ We compared this with the throughput of CO and CO₂, which we estimated from the partial pressures of these species and the speed of our pumping system. Within the accuracy of this measurement, we found that 100% of the sputtered C was converted to gaseous species and pumped away.

As a final test of this new cathode design, we placed a high-quality fused-silica substrate (witness plate) as close as possible to the cathode and exposed it to 80,000 consecutive PEPC shots. We compared the optical damage threshold before and after exposure to PEPC discharges and found that it was not significantly changed (we actually observed a slight increase in damage threshold after plasma exposure). During five months of operation in Beamlet, we have subjected the Beamlet PEPC to 50 to 60 high-fluence shots and 10,000 to 15,000 low-fluence alignment shots. We have not observed any reduction in damage threshold from plasma-related effects, proving the effectiveness of the C conversion process in actual use.

Crystal Heating

Most of the electrical energy used to drive the plasma discharges ends up as thermal energy deposited in the cathode surface by ion bombardment. The heated cathode heats the crystal, leading to a thermal gradient in the crystal. This causes strain in the crystal, which increases the depolarization of a beam traversing the PEPC. To quantify this depolarization, we removed the expansion optics from our polarimeter and illuminated a small spot on the crystal near the cathode side.

The results showed how the *ER* in this spot (normalized by the *ER* at the start of the test) decreases as the crystal heats. In one case, the simmer discharge was run continuously and dissipated 9 W at the cathode. The pulsed discharge, running at 0.25 Hz, adds another 3 W of average power. Under these conditions, the *ER* dropped to about 15% of its original value in only 30 minutes of continuous operation. In a second case, we reduced the average power dissipated by gating the simmer discharge on for only 100 ms for each shot. This reduces the average power due to the simmer discharge by a factor of 40. The average power from the pulsed discharge is unchanged, so the total average power for this case is 3 W. With the simmer discharge gated rather than running continuously, the *ER* only decreased to about 50 to 60% of its original value in a 30-minute operating period.

We measured heating in the PEPC by installing thermistors at five locations: center of the cathode, center of the E × B path (racetrack region) on the cathode, cathode edge of the crystal, anode edge of the crystal, and surface of the anode. Table 2 summarizes the temperature change at these locations after 100 minutes of operation. As expected, we observe maximum heating in the racetrack region, where the ion flux to the cathode is maximum. Heat conducts through the graphite to the rest of the cathode. The cathode edge of the crystal

exhibits more heating and depolarization than the anode edge. By gating the simmer, we reduced the temperature increase at the cathode edge of the crystal by a factor of 10.

As mentioned above, to further reduce crystal heating in the Beamlet PEPC, we increased the distance from the cathode to the crystal edge by mounting the cathode in a reentrant cavity. This design change, in combination with gating the simmer discharge, permits continuous operation of the Beamlet PEPC without significant thermal degradation of its switching performance.

Magnetic Bright Spots

During experiments with the prototype PEPC, we observed regions of nonuniform polarization rotation at various locations across the crystal. These regions show up as “bright spots” of light in the rejected polarization when imaging the PEPC in our polarimeter. In the PEPC, as originally constructed, we observed these bright spots along the bottom edge of the crystal, particularly in the lower corner near the anode. The bright spots were quite variable from shot to shot, indicating that they were due to a plasma-related effect and not a static optical effect.

We found that these bright spots are caused by the magnetic field surrounding wires carrying the discharge current external to the plasma. The discharge pulse is transmitted to the PEPC from the pulse generator via a pair of coaxial cables. The shields of these cables terminate at the anodes and the center conductors must connect to the cathodes. A magnetic field surrounds the unshielded sections of wire that traverse the PEPC. Figure 13 shows this magnetic field in a cross-sectional side view of the PEPC. The flux density from the current pulse is ≈ 60 G along the crystal edge near the wires. We verified that this was the cause of the bright spots by moving these wires from the bottom of the cell to the top. When we did this, the bright spots moved from the bottom anode corner to the top anode corner. We found that we could minimize bright spot formation by feeding the discharge current from opposite sides of the PEPC.

Our first explanation of the bright spots was as follows: Electrons carrying the switch-pulse current that charges and discharges the crystal must cross the magnetic field from the discharge wires, which is roughly perpendicular to the crystal surface; since plasma conductivity is lower across a magnetic field, charging and discharging is impeded. If this were a complete explanation, however, we would expect to see a bright spot across the full bottom edge of the image and not just in one corner. This simplistic model also does not explain why feeding current from opposite sides minimizes the bright spots. A better explanation for bright-spot formation will be a focus of future work.

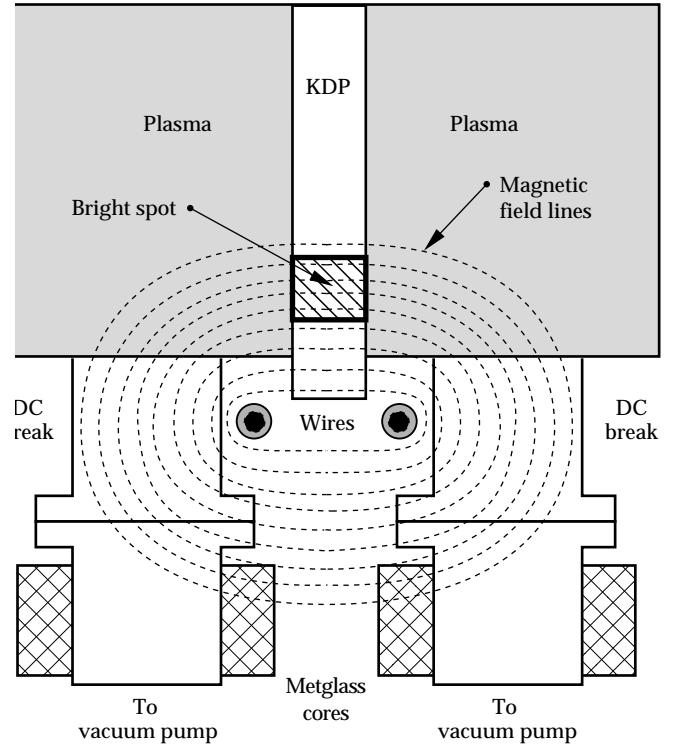


FIGURE 13. Cutaway end-view of the PEPC showing how the magnetic field from wires carrying the discharge current interferes with electron transport, and can therefore cause nonuniform switching. (70-50-0494-1852pb02)

TABLE 2. Heating (increases in $^{\circ}\text{C}$) due to plasma discharge at five locations inside the prototype PEPC, measured with thermistors.

	Cathode racetrack	Cathode center	Crystal (cathode edge)	Crystal (anode edge)	Anode
Continuous wave simmer	9.0	7.5	4.0	0.3	0.3
Gated simmer	0.7	0.5	0.4	0.25	0.25

Control of Switch-Pulse Leakage Current

The two sides of the PEPC are evacuated by a common vacuum system, most of which consists of metallic pipe sections held at ground potential. During the high-voltage switch pulse, leakage current can flow from the plasmas into the vacuum pipes. This effect is observable as droop in the switch pulse. We implemented two modifications to the original prototype design to control this leakage current (see Fig. 13): DC breaks and Metglass inductive isolators. The DC breaks are simply sections of vacuum line made of insulating material. The Metglass inductive isolators are toroids of tape-wound magnetic material that increase the inductance of the vacuum line for short pulses. During initial prototype experiments, we observed no switch-pulse droop, so we assumed that the leakage current was effectively controlled.

However, when we moved the discharge wires to the top of the cell, we observed a significant droop in the switch pulse. When the wires were on the bottom, the magnetic field surrounding them magnetized the DC breaks. The field in the breaks impeded electron flow, so we observed no leakage current. With the wires moved to the top of the cell, there was no field in the breaks. The leakage current was partially limited by the Metglass cores, but the droop was not acceptable.

One way to reduce the droop would have been to increase the inductance by increasing the cross-sectional area of Metglass. We used a more effective and less expensive solution: We mounted a pair of baffles inside the vacuum port and in the region of the DC break. This increases the effective path length through the DC breaks. The baffles also block the line of sight for electron flow and increase the wall area on which plasma can be neutralized. The resulting increase in isolation is enough to eliminate the switch-pulse leakage current.

The baffles also reduce the vacuum conductance through the DC breaks, which increases the base pressure but reduces the required flow of working gas to maintain the operating pressure. The increase in base pressure with one pair of baffles did not reduce switching performance, but the increase with two pairs of baffles on each side was high enough to reduce performance noticeably.

Estimation of Plasma Density

Plasma density and temperature produced during PEPC operation are required to compute the plasma resistance. Our estimation of these parameters is based

on the observation that the switch-pulse voltage required to induce 90° of polarization rotation is consistently higher than the known half-wave voltages for KDP and KD*P. We also observe that if we increase the discharge current, lower applied switch-pulse voltage is required, and vice versa. This indicates that the voltage appearing across the crystal depends on plasma density. Since the current in the switch-pulse circuit drops to zero after initial charging, there can be no resistive voltage drops. Voltage not appearing across the crystal must be appearing across other capacitive elements that form a capacitive voltage divider. In this case, the extra capacitance comes from the plasma sheaths that form at the interface between the plasma and the crystal. The voltage divider expression is

$$V_{\pi} = V_{sw} \frac{C_{sheath}}{C_{KDP} + C_{sheath}}, \quad (4)$$

where $V_{\pi} = 16.4$ kV and is the clamped half-wave voltage for KDP,⁶ $V_{sw} = 18.1$ kV and is the switch-pulse voltage required for 90° rotation, $C_{KDP} = 1.81$ nF and is the capacitance of the $32 \times 32 \times 1$ cm³ KDP crystal, and C_{sheath} is the sheath capacitance. Solving for C_{sheath} and inserting numerical values, we find $C_{sheath} = 17.5$ nF. If we assume that similar sheaths form on each side of the crystal, then the capacitance for each sheath is 35 nF.

To relate the sheath capacitance to the plasma density and temperature, we start with an expression for the potential, $\phi(x)$, in an infinite, planar sheath:

$$\phi(x) = \phi_0 e^{\pm x/\lambda_D}, \quad (5)$$

where λ_D is the Debye length given by

$$\lambda_D = 740 \sqrt{\frac{T_{eV}}{n_e}}. \quad (6)$$

The electric field in the sheath is then given by

$$E = \frac{d\phi}{dx} = -\frac{\phi_0}{\lambda_D} e^{\pm x/\lambda_D}. \quad (7)$$

The energy W stored in the electric field is then

$$W = \frac{\epsilon_0}{2} \int E^2 dv = \frac{A\epsilon_0}{2} \frac{\phi_0^2}{\lambda_D^2} \int_0^\infty e^{\pm 2x/\lambda_D} dx = \frac{A\epsilon_0\phi_0^2}{4\lambda_D}, \quad (8)$$

where A is the area of the crystal and the sheaths and ϵ_0 is the dielectric constant of vacuum. The stored electrostatic energy can also be expressed in terms of capacitance C_{sheath} by

$$W = \frac{1}{2} C_{sheath} \phi_0^2. \quad (9)$$

Equating the expressions for W and solving for C , we obtain

$$C_{\text{sheath}} = \frac{A\epsilon_0}{2\lambda_D}, \quad (10)$$

which is the expression for the capacitance of a parallel-plate capacitor of area A and separation $2\lambda_D$. Note that we use the dielectric constant for vacuum in the above expressions. Although a region filled with plasma has a modified dielectric constant, most of the sheath electric field is in the region closest to the crystal, where the electron density is very low, so the use of ϵ_0 is a good approximation. We substitute Eq. (6) for the Debye length in Eq. (10) and solve for the electron density, obtaining

$$n_e = 3.3 \times 10^{11} T_e. \quad (11)$$

For the expected range of electron temperature (1 to 10 eV), the plasma density is then in the range 3.3×10^{11} to 3.3×10^{12} .

Conclusion

In the technology of PEPCs, plasma discharges facilitate uniform application of voltage to large-aperture, thin, electro-optic KDP crystals. PEPC technology makes possible the construction of large-aperture optical switches for use in high-energy ICF laser drivers. After building and testing a $32 \times 32 \text{ cm}^2$ prototype PEPC with KDP and KD*P crystals, we built a $37 \times 37 \text{ cm}^2$ PEPC with a KDP crystal for use in the Beamlet laser. The Beamlet PEPC routinely switches a 5- to 6-kJ, 3-ns optical pulse out of the amplifier cavity after four gain passes. The Beamlet PEPC has demonstrated switching efficiency >99.5% and has operated reliably during Beamlet experiments.

We also discuss PEPC technology issues, including cathode sputtering, cathode heating, and magnetic

bright spots. We control deposition of sputtered cathode material by using graphite cathodes and adding oxygen to the plasma; the oxygen reacts with sputtered carbon to form gaseous species. We control cathode heating by reducing the average discharge power with a gated simmer discharge and by moving the cathode further from the crystal. Magnetic fields from the discharge current can cause spatial nonuniformities in the switching profile. We control this effect by feeding the side 1 and side 2 discharge currents from opposite sides to reduce stray magnetic fields. Finally, we show that we can estimate the plasma density from the extra capacitance caused by sheath formation between the plasma and the crystal.

Notes and References

1. J. R. Murray, J. H. Campbell, D. N. Frank, J. T. Hunt, and J. B. Trenholme, *ICF Quarterly Report*, 1 (3), 89–107, Lawrence Livermore National Laboratory, Livermore, CA, UCRL-LR-105821-91-3 (1991).
2. L. L. Steinmetz, T. W. Pouliot, and B. C. Johnson, *Appl. Opt.* 12, 1469–1471 (1973).
3. M. D. Skeldon, M. S. Jin, D. J. Smith, and S. T. Bui, *Solid State Lasers II*, SPIE 1410, 116–124 (1991).
4. J. Goldhar and M. A. Henesian, *IEEE J. Quantum Electron.* QE-22, 1137–1147 (1986).
5. D. Eimerl, *Ferroelectrics* 77, 95–159 (1987).
6. M. A. Rhodes, J. J. DeYoreo, B. W. Woods, and L. J. Atherton, *ICF Quarterly Report* 2 (1), 23–36, Lawrence Livermore National Laboratory, Livermore, CA, UCRL-LR-105821-92-1 (1992).
7. Microsim Corporation, Irvine, CA.
8. D. E. Golden and H. W. Bandel, *Phys. Rev. J1* V138, 14 (1965).
9. F. F. Chen, *Introduction to Plasma Physics*, Plenum Press, New York, p. 162.
10. C. A. Ebberts, J. Happe, N. Nilson, and S. P. Velsko, *Appl. Opt.* 31, 1960–1964 (1992).
11. J. J. DeYoreo and B. W. Woods, *J. Appl. Phys.* 73, 7780 (1993).
12. I. M. Thomas, *Optics News*, 18–22, (August 1986).
13. R. K. Waits, *J. Vac. Sci. Technol.* 15, 179, (1978).
14. M. A. Rhodes and J. Taylor, *Twentieth Power Modulator Symposium*, IEEE CH3180-7, 380 (1992).
15. B. M. VanWanterghem, J. R. Murray, D. R. Speck, and J. H. Campbell, *Proc. Eleventh Topical Meeting on the Technology of Fusion Energy*, New Orleans, LA, 1994.
16. D. Rosen and G. K. Wehner, *J. Appl. Phys.* 33, 1842–1845 (1962).